RSC Advances

PAPER

View Article Online
View Journal | View Issue

Cite this: *RSC Adv.*, 2022, **12**, 29793

Compositing of MOFs with ceramic and nanoparticles for efficient and rapid adsorptive desalination of artificial seawater or NaCl solution

Irfan Ijaz, *[a] Aysha Bukhari,[a] Ezaz Gilani,[a] Ammara Nazir[a] and Hina Zain[b]

Received 6th July 2022
Accepted 11th October 2022

DOI: 10.1039/d2ra04182k

rsc.li/rsc-advances

Poor water availability with the fast-growing population creates crucial issues for universal water security, and efficient approaches ought to be accomplished to balance the demand and supply. One of the most energy- and cost-effective methods for removing NaCl is adsorption desalination. Metal–organic frameworks with ceramic and nanoparticles are a comparatively new research route that increases the desalination capacity. The synthesized composites were examined for efficient and rapid removal of NaCl from NaCl solution or artificial seawater. The adsorption desalination properties were analyzed based on adsorption isotherm, adsorption kinetics, contact time, NaCl, and adsorbent dosage. The adsorptive desalination rate of ZnO@MIL88A(Fe)@α-cordierite composite was only decreased by 4% as the maximum loss after 5 consecutive cycles.

1. Introduction

One of the well-known global challenges of the twenty-first century is water scarcity. Due to overexploitation, growing industrialization, climate change, and population increase, current water supplies are insufficient.[1] As per the United Nations, nearly 7 billion people in 60 countries will face extreme water scarcity by 2050.[2–4] One of the most effective and ancient technologies for meeting the growing need for high quality water is the desalination of seawater.[5,6]

Traditionally, there are now two types of desalination technologies such as membrane-based and thermal desalination. In the membrane-based desalination approach, salt is separated from freshwater by selective permeability of the permeable membrane. Membrane-based desalination is divided into capacitive deionization, reverse osmosis, and capacitive deionization.[7–10] Thermal desalination is carried out using condensation, evaporation, and heating to derive drinkable water. Thermal desalination includes multiple-effect distillation and multi-stage flash.[8,11–13] Furthermore, such energy-intensive desalination approaches demand very high maintenance and operation expenses.[14] For instance, membrane-based reverse osmosis encounters issues like membrane fouling, scaling, and high operating pressure.[15,16] Adsorption is a well-known phenomenon that requires little external energy to perform. The adsorption process is flexible, easy to run, energy efficient, and inexpensive. Due to these advantages, adsorption has emerged as a highly innovative and attractive approach for water desalination and purification. Nowadays, MOFs emerge as an advanced multidimensional infinite category of porous polymers consisting of metal or a group of metals and organic ligands. MOFs attain remarkable attention from researchers and scientific societies due to their high porosity, controllable morphological traits, and remarkable advantages in the domain of photocatalysis, photoluminescence, adsorption, and separation.[17–19] Even though hundreds of new metal–organic frameworks have been prepared and published by researchers and scientific societies in the last two decades for utilization in a wide range of applications, only a small quantity has been commercialized, and the greater digit of MOFs exhibit disadvantages and limitations like hydrothermal, or thermal instability, high production expense, and chemical.[20] Incorporation of MOFs with other substances is an advanced route that provides the solution to these issues. Fabrication of MOFs composites exhibits good performances in various applications due to the textural and structural trait.[21]

Fe-based MOFs have been broadly used for heavy metal adsorption. In MIL88A(Fe), iron is linked with a fumarate linker, and formed a 3D framework with interlinked cages and pores, which showed good adsorption capacity.[22,23]

Surprisingly, there are limited publications on composites of MOFs with ceramics. Porous ceramics have been utilized as catalysis and filters, and adsorption materials.[24]

Herein, the primary aim of this research is to the rapid removal of NaCl from artificial seawater or NaCl solution using nZnO@MIL88A(Fe)@α-cordierite composites. For this objective, we introduced two essential features, such as porosity and positive and negative charge in the synthesized material using ZnO Nps, α-cordierite ceramics, and MIL88A(Fe) MOFs. α-

[a]*School of Chemistry, Faculty of Basic Sciences and Mathematics, Minhaj University Lahore, Lahore 54700, Pakistan. E-mail: iffichemixt266@gmail.com*

[b]*Department of Allied Health Sciences, Superior University Lahore, Lahore 54700, Pakistan*

cordierite ceramics is negatively charged, and MIL88A(Fe) MOFs and ZnO NPs are positively charged in the nZnO@MIL88A(Fe)@α-cordierite composites. Positive and negative charges on composites attract the Na^+ and Cl^- simultaneously. The total number of pores is increased by mixing ZnO Nps, α-cordierite ceramics, and MIL88A(Fe) MOFs, which further enhance the adsorptive desalination of NaCl. The adsorptive desalination rate of ZnO@MIL88A(Fe)@α-cordierite composites was compared with α-cordierite and MIL88A(Fe). The prepared ZnO@MIL88A(Fe)@α-cordierite composite exhibited an excellent adsorptive desalination capacity.

2. Materials and methods

2.1. Materials

All of the apparatus utilized in this study had standard quick-fit joints and were dried at 100 degrees Celsius. The chemicals for this work were commercial sea salt, water deionized (DI) (Merck), fumaric acid (Merck), iron nitrate (Merck), ethanol (Merck), aluminum nitrate (Merck), magnesium nitrate (Merck), ethylene glycol (Merck), citric acid (Merck) and silica (Merck). The plant was collected from local a nursery in Punjab province Lahore.

2.2. Greener-microwave assisted synthesis of ZnO@MIL88A(Fe)@α-cordierite composites

Syzygium Cumini aqueous leaves extract was made by mixing 50 g of *Syzygium cumini* leaves powder with 200 mL of DI water to make the leaves extract. The reaction solution was continuously stirred while boiling at 60 °C for 20 minutes. A clear solution was obtained by filtering the yellowish mixture. This clear solution was to keep it at 4 degrees Celsius for subsequent processing. To synthesize the ZnO nanoparticles, 50 mL of aqueous leaves extract of *S. cumini* was warmed at 60 °C. Then, 5 g of Zin acetate salt was mixed by utilizing a magnetic stirrer. The mixture was stirred continuously for 4 hours until the ZnO precipitates formed. Finally, the prepared precipitates of ZnO were transferred to the oven at 90 degrees Celsius for 3 hours to calcine it.

15 mM fumaric acid solution was combined with 15 mL iron nitrate solution to make MIL88A(Fe). The reaction mixture was then placed into an electric furnace and warmed until precipitated formed that collected by filtration and cleaned with deionized water five times and then dried in a furnace at about 50 °C. The filtration process was used to collect the precipitates, and obtained precipitates were then washed three times with water and dried at 70 °C. Deposition of MIL88A (Fe) on the ZnO nanoparticles was achieved by dispersing 0.10 g of ZnO nanoparticles in a 15 mM of ethanol solution, and 15 mM of fumaric acid, and heating for about 5 minutes, and the resulting product was nZnO@MIL88A(Fe).

α-cordierite porous powder (ceramics) was prepared by using the process reported by.[25,26] nZnO@MIL88A(Fe)@α-cordierite composites were prepared by mixing 2 g of ZnO@MIL88A(Fe) with 2 mL of cordierite aqueous solution under microwave irradiation for 5 minutes. The prepared nZnO@MIL88A(Fe)@α-cordierite composites were cleaned with ethanol solution and dried at 45 °C. Positively charged MOFs bind with negatively charged oxygen of ceramics and form stable composites as demonstrated in Fig. 1.

2.3. Adsorptive desalination experiment

Synthesized porous ceramic, MOF, and composites can adsorb the negative and positive ions dissolved in saline or seawater. 5–20 g of MIL88A(Fe) MOF, α-cordierite porous, and nZnO@MIL88A(Fe)@α-cordierite composites were poured into a round bottom flask and interacted with 15 mL of artificial seawater or brine solution (Lahore) in all studies except the dose influence test. Commercial sea salt was dissolved to create an artificial seawater solution. The prepared brine solution will be utilized in future experiments in this work. When the MOF, ceramic, and composites interact with a sample, fluctuation in the

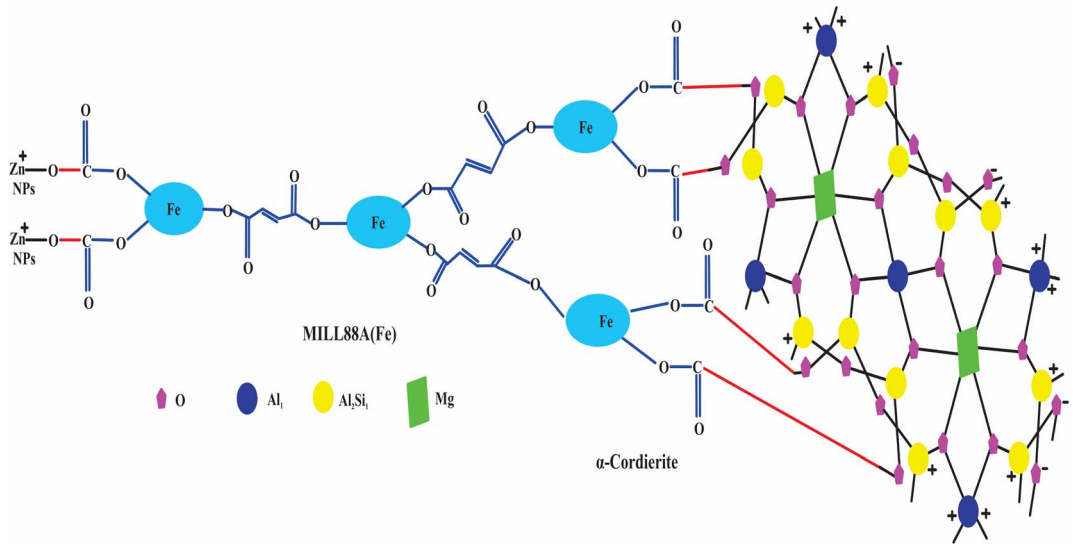

Fig. 1 Possible mechanism for synthesis of nZnO@MIL88A(Fe)@α-cordierite composites.

electro-conductivity of the sample was determined by utilizing an electro-chemistry meter. The difference in electrical conductivity implies that the adsorbents have reduced ion concentration. Hence, the determined electrical conductivity values offer quantitative data on desalination.

$$R(\%) = \left(C_i - \frac{C_t}{C_i}\right) \times V \quad (1)$$

$$q_e = \left(C_i - \frac{C_e}{m}\right) \times V \quad (2)$$

C_i (mg L^{-1}) denotes the initial dosage, and C_e (mg L^{-1}) describes the final dosage of ions in artificial seawater. V defines the net volume in L and m defines the number of adsorbents in g of brine solution.

A stoichiometric quantity of MOFs, ceramic, and composites was composed of each round bottom flask to examine the disilane performance. The sorption kinetics was examined by utilizing 15 mL of sodium chloride at 12 000 mg L^{-1} concentration and 7 g of each adsorbent (MIL88A(Fe) MOF, α-cordierite porous, and nZnO@MIL88A(Fe)@α-cordierite composites). The adsorptive desalination rate of 6000, 12 000, 18 000, and 24 000 mg L^{-1} sodium chloride solutions were evaluated to investigate the effect of adsorbate dosage. For 2.0, 4.0, 6.0, 8.0, and 10.0 g of MOF, ceramic, and composites in 15 mL of 24 000 mg L^{-1} sodium chloride solution for 13 minutes, change in adsorptive desalination rate were determined according to adsorbent dosage. 15 mL of 12 000 mg L^{-1} NaCl solution and 7 g of MIL88A(Fe) MOF, α-cordierite porous, and nZnO@MIL88A(Fe)@α-cordierite composites were employed in the adsorption isotherm experiment. The adsorptive desalination was investigated in all of these studies using NaCl solution. The possible mechanism of adsorptive desalination is exhibited in Fig. 13.

2.4. Adsorption–desorption study

To employ the prepared nZnO@MIL88A(Fe)@α-cordierite composites for practical applications, it is necessary to determine what kind of consequences can be predicted when the composites are exposed to seawater. Thus, an adsorption–desorption analysis was carried out by utilizing 15 mL of Nacl solution or artificial seawater and 7 g of prepared nZnO@MIL88A(Fe)@α-cordierite composites. The adsorption–desorption analysis was carried out for 160 min. The composites that absorbed NaCl ions were bathed in deionized water after each cycle and reused.

3. Result and discussion

3.1. Characterizations of synthesized ZnO NPs, MIL88A(Fe),α-cordierite porous ceramic, and nZnO@MIL88A(Fe)@α-cordierite composites

3.1.1. XRD analysis. The XRD pattern of ZnO NPs, MIL88A(Fe), α-cordierite porous ceramic, and nZnO@MIL88A(Fe)@α-cordierite composites are exhibited in Fig. 2. The

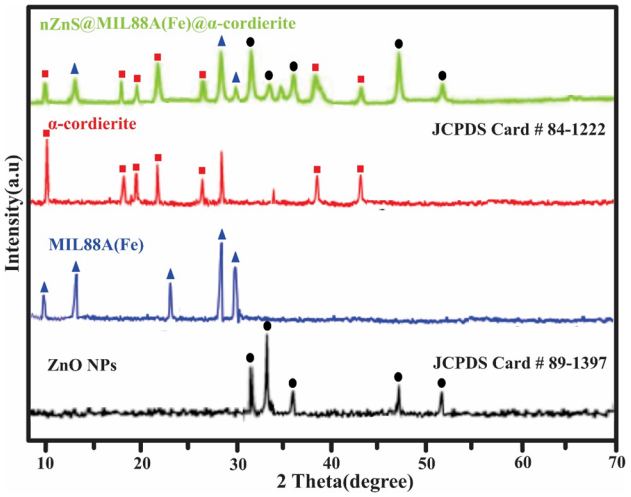

Fig. 2 XRD Patterns of ZnO NPs, MIL88A(Fe) MOFs, α-cordierite porous ceramic, and nZnO@MIL88A(Fe)@α-cordierite composites.

XRD peaks were aligned well with zinc oxide nanoparticles and indexed with JCPDS card number # 89–1397. In case of MIL88A(Fe), X-ray diffraction patterns indicated a series of narrow, well-defined reflections (2 theta = 10–32°), indicating a crystalline phase. Furthermore, the placements of all peaks in the MIL88A(Fe) MOFs were similar to previously prepared MIL88A(Fe),[27] ensuring that the MOFs were successfully prepared. XRD pattern of α-cordierite porous was seen to be well in agreement with JCPDS card number # 84–1222. In the XRD pattern of ZnO@MIL88A(Fe)@α-cordierite composite, we can observe characteristic peaks of ZnO NPs, MIL88A(Fe) MOF, and α-cordierite ceramic which confirmed the synthesis of nZnO@MIL88A(Fe)@α-cordierite composites. However, the crystallinity and peaks of composites were slightly weak as compared to the individual materials. This phenomenon was due to the preparation of an amorphous product formed by the mixing of ZnO NPs, MIL88A(Fe) MOF, and cordierite ceramic.

3.1.2. FTIR analysis. The FTIR spectrum of ZnO nanoparticles, MIL88A(Fe) MOFs, α-cordierite porous ceramic, and nZnO@MIL88A(Fe)@α-cordierite composites are exhibited in Fig. 3. For ZnO nanoparticles, the bands manifested at 435 and 616 cm^{-1} are assigned to the typical stretching mode of the Zn–O bond.[28,29] The band that appeared at 3189 cm^{-1} is attributed to the MIL88A(Fe) and a similar band was reported by.[30] For α-cordierite ceramic, the signals appeared at 1169 and 859 cm^{-1} attributed to AlO_4 and SiO bonds.[31,32] The band manifested at 1077–1090 cm^{-1} is based on the existence of Si–O vibration of non-crystalline silica powder. In the structure of nanocrystalline-cordierite, these peaks drop to lower levels, indicating the generation of Si–O–Mg or Si–O–Al bonds.[33,34] The bands that appeared at 745, 520, and 460 cm^{-1} are attributed to $MgAl_2O_4$, MgO_6, and TiO_2.[35–37] FTIR bands of nZnO@MIL88A(Fe)@α-cordierite composite were well matched ZnO nanoparticles, MIL88A(Fe) MOFs, and α-cordierite porous ceramic and confirmed the synthesis of and nZnO@MIL88A(Fe)@α-cordierite composites.

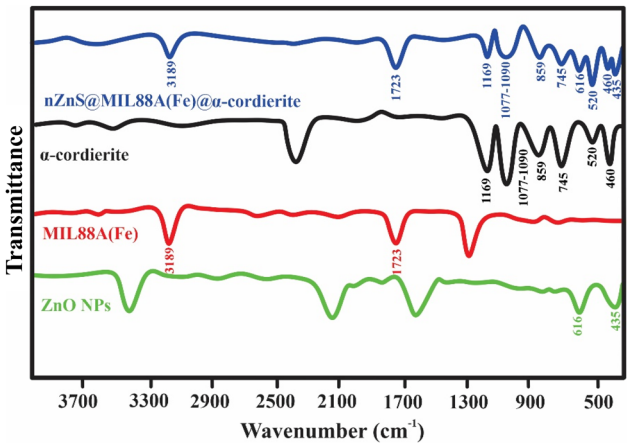

Fig. 3 FTIR patterns of ZnO NPs, MIL88A(Fe) MOFs, α-cordierite porous ceramic, and nZnO@MIL88A(Fe)@α-cordierite composites.

3.1.3. SEM analysis. The SEM micrograph of ZnO nanoparticles, MIL88A(Fe) MOF, α-cordierite porous ceramic, and nZnO@MIL88A(Fe)@α-cordierite composites were examined as exhibited in Fig. 4. Fig. 4(a) exhibited the spherical shape of MIL88A(Fe) MOFs in the range of 31–37 nm. Fig. 4(b) exhibited an irregular shape of ZnO Nps in the range of 40–49 nm. ZnO NPs and MIL88A(Fe) MOF exhibited a mesoporous (2–50 nm) range of particles. Fig. 4(c) exhibited the spherical shape of α-cordierite porous ceramic in the range of 2–11 nm. The α-cordierite porous ceramic exhibited a micropores (0–2 nm) range of particles. nZnO@MIL88A(Fe)@α-cordierite composites exhibited agglomerated heterogeneous shapes. Fig. 4(d) exhibited spherical and irregular of shapes micro and mesoporous particles. The spherical shape particles are derived from MOF and α-cordierite, and irregular is particles derived from ZnO NPs.

3.1.4. BET analysis. The BET isotherm of synthesized ZnO nanoparticles, MIL88A(Fe) MOFs, α-cordierite porous ceramic, and nZnO@MIL88A(Fe)@α-cordierite composites are exhibited in Fig. 5(a–d). The BET isotherm of synthesized ZnO nanoparticles, MIL88A(Fe) MOF, α-cordierite porous ceramic, and nZnO@MIL88A(Fe)@α-cordierite composites resembled the IUPAC classification Type I and IV. Its mean samples have two types of structures (micropores and mesoporous). nZnO@MIL88A(Fe)@α-cordierite composites showed a micro-meso hybrid (I/IV) form of isotherm, micropore (0–2 nm) obtained from α-cordierite whereas mesoporous (2–50 nm) pore obtained from ZnO Nps and MIL88A(Fe) MOF during the formation of composites as shown in Fig. 5(a, c and d). The nonlocal density functional theory (NLDFT) model, was also used to analyze the

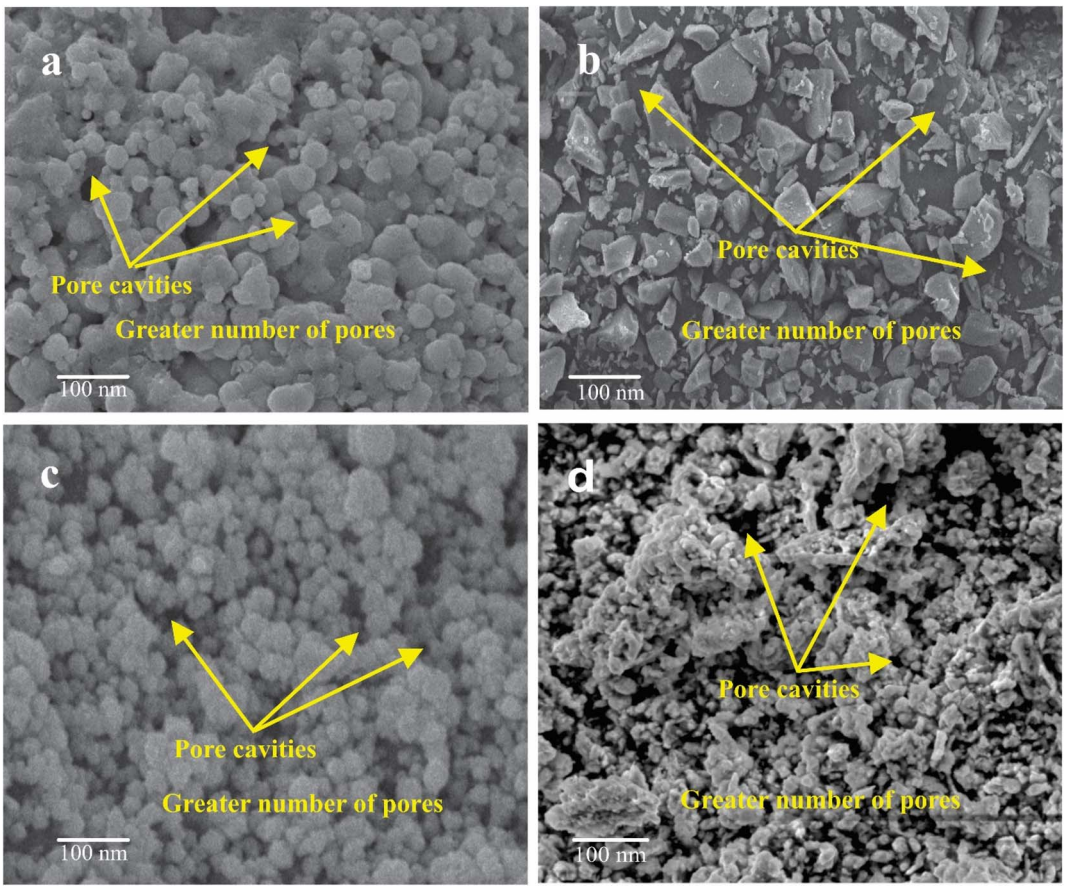

Fig. 4 SEM images of MIL88A(Fe) MOFs (a), ZnO NPs (b), α-cordierite porous ceramic (c), and nZnO@MIL88A(Fe)@α-cordierite composites (d) before adsorptive desalination.

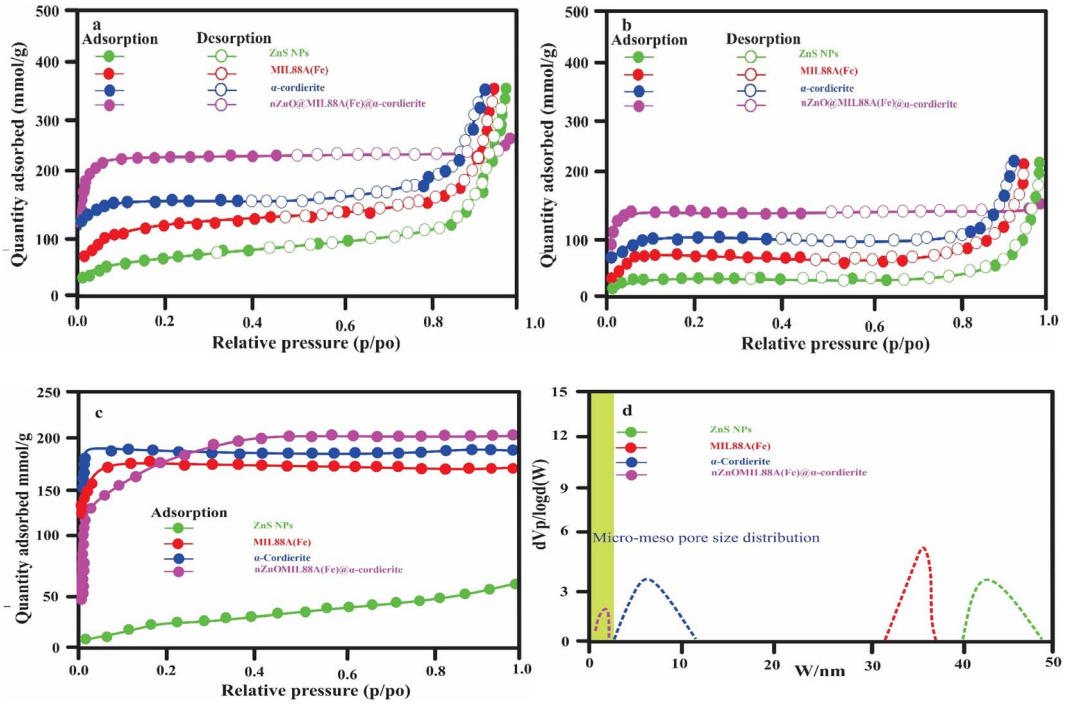

Fig. 5 N2 adsorption–desorption plot of MIL88A(Fe) MOFs, ZnO NPs, α-cordierite porous ceramic, and nZnO@MIL88A(Fe)@α-Cordierite composites before (a) and after (b) after desalination. (c) N2 simulated sorption plot of MIL88A(Fe) MOFs, ZnO NPs, α-cordierite porous ceramic, and nZnO@MIL88A(Fe)@α-cordierite composites by NLDFT model. (d) Micro-mesopore size distribution for MIL88A (Fe) MOFs, ZnO NPs, α-cordierite porous ceramic, and nZnO@MIL88A(Fe)@α-cordierite composites.

pore size distribution of MIL88A(Fe) MOFs, ZnO NPs, α-cordierite porous ceramic, and nZnO@MIL88A(Fe)@α-cordierite composites. The pore size distribution plots and obtained N2 isotherms after Gaussian fitting is exhibited in Fig. 5(c). The prepared composites had a very high N2 adsorption capacity at low pressure. This could be described by the preparation of a new composite with micropore, formed as the result of a combination of ZnO nanoparticles, MIL88A(Fe) MOFs, and α-cordierite porous ceramic. Table 1 summarizes the results for the measured surface area and pore volume of ZnO nanoparticles, MIL88A(Fe) MOF, α-cordierite porous ceramic, and nZnO@MIL88A(Fe)@α-cordierite composites before and after adsorptive desalination. The BET analysis after adsorptive desalination of NaCl on the ZnO nanoparticles, MIL88A(Fe) MOFs, α-Cordierite porous ceramic, and nZnO@MIL88A(Fe) @α-Cordierite composites were performed. As displayed in Fig. 5(b), the N2 adsorption–desorption isotherm of ZnO nanoparticles, MIL88A(Fe) MOFs, α-cordierite porous ceramic, and nZnO@MIL88A(Fe)@α-cordierite composites before or after adsorptive desalination of NaCl were almost similar in the hysteresis loop's shape with a minor difference, which can be attributed to the adsorptive desalination of NaCl inside the pores cavities of all samples. Consequently, the surface areas of ZnO NPs, MIL88A(Fe) MOFs, α-cordierite porous ceramic, and nZnO@MIL88A(Fe)@α-cordierite composites were decreased after adsorptive desalination due to the filling of pore cavities by NaCl as exhibited in SEM images.

3.1.5. Stability of nZnO@MIL88A(Fe)@α-cordierite composites. The zeta potential is used to examine the stability and surface charge of the materials. Fig. 6 (a–d) exhibited the zeta potential of ZnO NPs, α-cordierite porous ceramic, MIL88A(Fe), and nZnO@MIL88A(Fe)@α-cordierite composites,

Table 1 Particles size, and average pore volume, surface area (before and after adsorption) of MIL88A(Fe) MOFs, ZnO NPs, α-cordierite porous ceramic, and nZnO@MIL88A(Fe)@α-cordierite composites

Sample	Average particles size (nm)	Average pore volume (cm^{-3} g^{-1})	Average surface area (m^2 g^{-1}) before adsorption	Average surface area (m^2 g^{-1}) after adsorption
ZnO	40–49	2.9	163	55
α-Cordierite porous	2–11	4.0	319	181
MIL88A(Fe) MOF	31–37	3.2	232	139
nZnO@MIL88A(Fe)@ α-cordierite composites	0.5–1.8	7.6	457	216

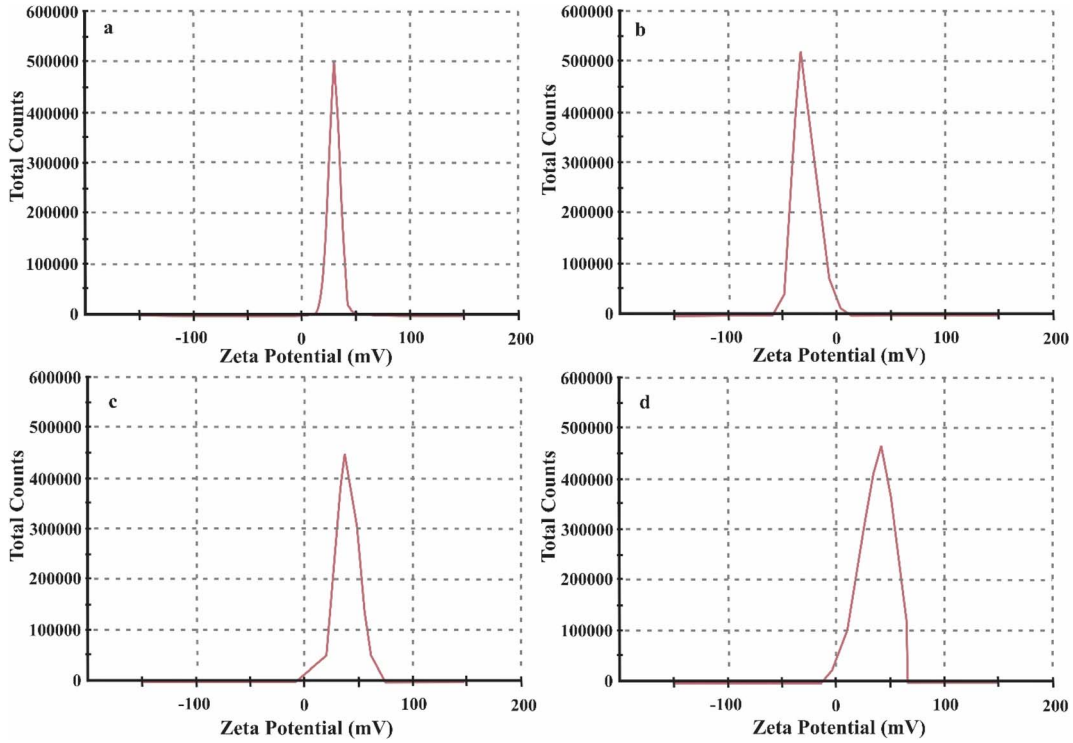

Fig. 6 Zeta potentials of ZnO NPs (a), α-cordierite porous ceramic (b), MIL88A(Fe) (c), and nZnO@MIL88A(Fe)@α-cordierite composites (d).

respectively. The zeta potential of ZnO nanoparticles and MIL88A (Fe) were close to +33 and +40 mV, whereas the zeta potential of α-Cordierite was −42 mV. The appearance of positive [ZnO and MIL88A(Fe)] and negative potential indicates the relatively stable interaction between positively charged ZnO and MIL88A(Fe) and negatively charged α-cordierite. The zeta potential of nZnO@MIL88A(Fe)@α-cordierite composites was 49 mV. Zeta potential having value may be negative or positive, but greater than +30 or −30 mV favors the stability of materials. The zeta potential of prepared nZnO@MIL88A(Fe)@α-cordierite composites was greater than 30 mV and hence, stable.[38]

3.2. Adsorptive desalination of NaCl by MIL88A(Fe) MOFs, α-cordierite porous ceramic, and nZnO@MIL88A(Fe)@α-cordierite composites

3.2.1. Influence of adsorbents dosage. Fig. 7(a and b), indicates the influence of adsorbent dose in 12 000 mg L^{-1} salt solution. The adsorption capacity decreased when the concentration of the adsorbents (MIL88A(Fe) MOFs, α-cordierite porous, and nZnO@MIL88A(Fe)@α-cordierite composites) was increased. Initially, as the minor quantity of prepared adsorbents interacts with salt solution, the prepared adsorbents will be readily saturated because of the availability of the excess concentration of NaCl solution or artificial seawater. Moreover, as the dosage of MIL88A(Fe) MOFs, α-cordierite porous, and nZnO@MIL88A(Fe)@α-cordierite composites increased, the number of pore sites also rose in comparison to the limited number of NaCl ion. This rise in the number of unsaturated pore sites decreased the adsorptive desalination Capacity.

3.2.2. Influence of NaCl dosage. The influence of NaCl solution dosage on adsorptive desalination is indicated in Fig. 7(c). The highest adsorptive desalination was indicated at 80%, 87%, and 98% by MIL88A(Fe) MOFs, α-cordierite porous, and nZnO@MIL88(Fe)@α-cordierite composites respectively when the dosage of NaCl solution is 12 000 mg L^{-1}. The adsorptive desalination rate was increased as the NaCl solution dosage increased because MIL88A(Fe) MOF, α-cordierite ceramic, and nZnO@MIL88A(Fe)@α-cordierite composites have greater chances of salt solution. When the MOFs, ceramic composites come into contact with a NaCl solution with a dosage greater than 12 000 mg L^{-1}, the adsorptive desalination rate decreases as the concentration rise. This decrease in desalination rate was due to the saturation of pores sites or coordination sites of MIL88A(Fe) MOFs, α-cordierite ceramic, and nZnO@MIL88A(Fe)@α-cordierite composites. Fig. 7(a) indicated that nZnO@MIL88A(Fe)@α-cordierite composites showed a greater desalination rate than MOFs and ceramics. This result from the greater number of pores site on composites than on MOFs and ceramics. The number of pore sites on nZnO@MIL88A(Fe)@α-cordierite composites is equal to the sum of the pores of MOFs and ceramics. Thus, nZnO@MIL88A(Fe)@α-cordierite composites exhibited the highest adsorptive desalination rate.

3.2.3. Influence of particles size. Fig. 7(d) indicates the influence of particle size MOF, ceramics, and composites on adsorptive desalination. Fig. 3 indicates that adsorptive desalination increases as particle size decreases. Surface area increases as particle size decrease. Thus, the adsorptive

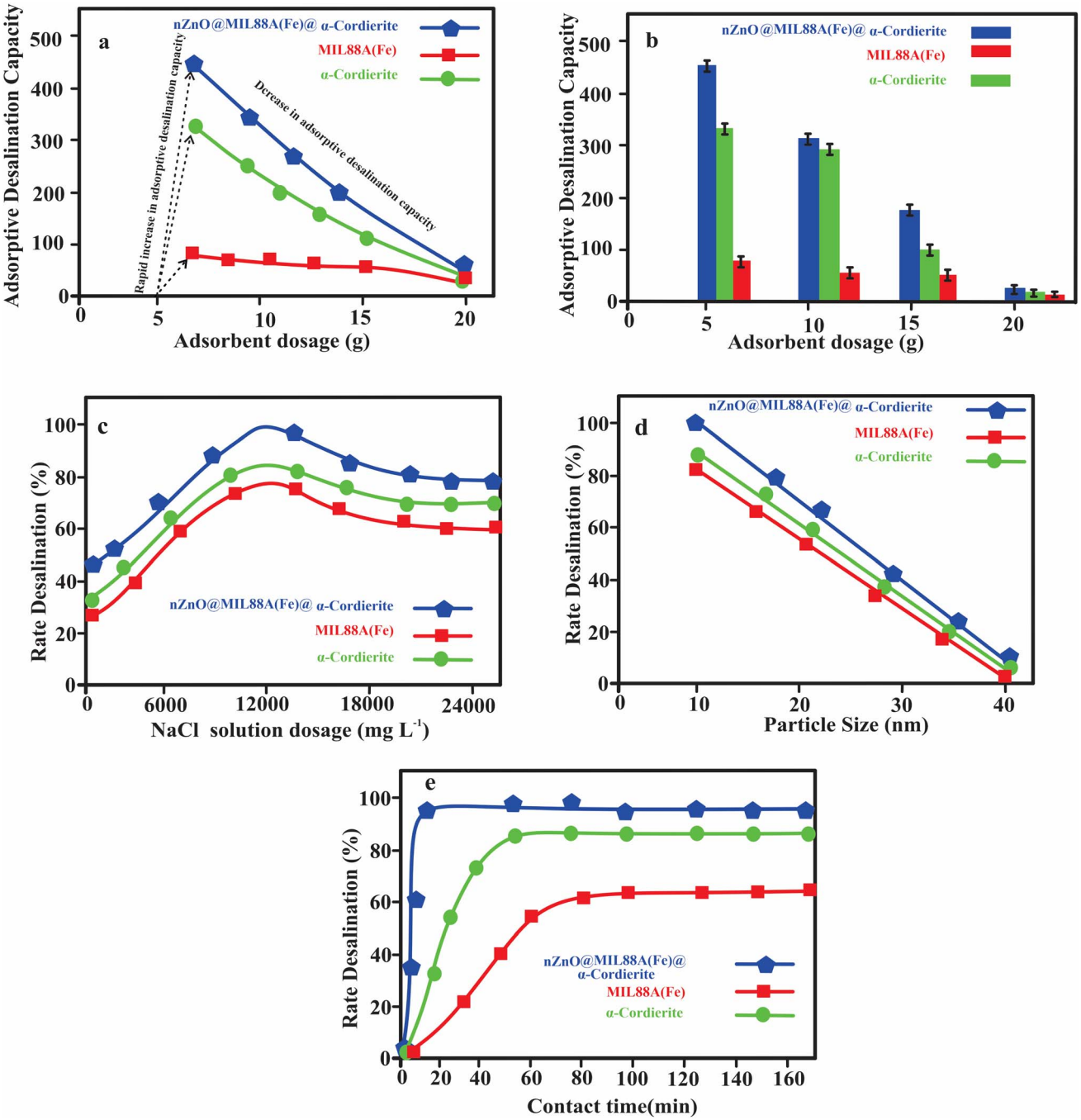

Fig. 7 Influence of adsorbent dosage (a and b), influence of NaCl solution dosage (c), influence of particles size (d), and contact time (e) on desalination rate.

desalination rate increases with a decrease in particle size. Fig. 7(d) also showed that nZnO@MIL88 (Fe)@α-cordierite composites had a greater rate of adsorptive desalination than MIL88A(Fe) MOFs and α-cordierite. This fact can be described by using the results of BET analysis, the particles size (0.5–8 nm) of nZnO@MIL88A(Fe)@α-cordierite composites was less than the size of MIL88A(Fe) MOFs (2–11 nm) and α-cordierite (35–47 nm). Thus, nZnO@MIL88A(Fe)@α-cordierite composites exhibited higher adsorptive desalination than MIL88A(Fe) MOFs and α-cordierite ceramic.

3.2.4. Contact time. The total desalination rate of the anions (Na^+) and cations (Cl^-) were the same, and both reached adsorptive desalination equilibrium at the same time. nZnO@MIL88A(Fe)@α-cordierite composites reached desalination equilibrium in 13 minutes, whereas α-cordierite and MIL88A(Fe) reached equilibrium in 57 and 91 minutes, respectively as exhibited in Fig. 7(e). The greater surface area and higher numbers of pore sizes enhanced the diffusion of cationic and anionic ions to composites, resulting in rapid desalination. nZnO@MIL88A(Fe)@α-cordierite composites

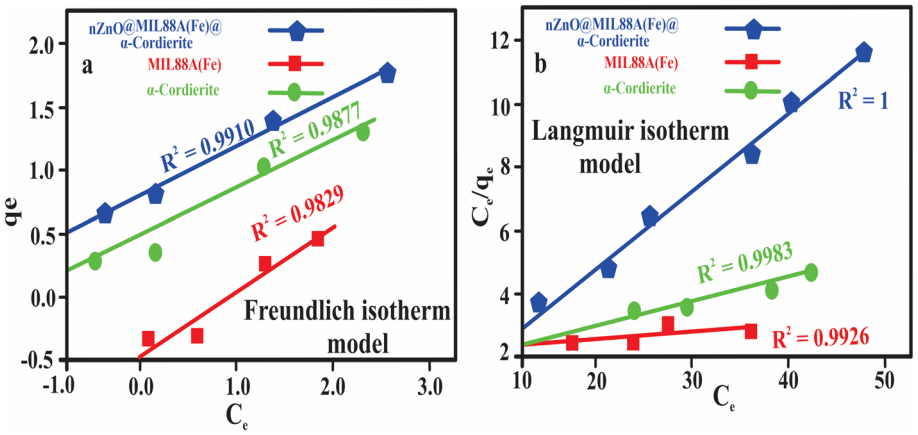

Fig. 8 Isothermal study, Langmuire isotherm model (a), and Freundlich isotherm model (b).

have a greater surface area and higher number of pores than α-cordierite and MOF (according to Table 1). Thus, composites reached earlier adsorptive desalination equilibrium than the ceramic and MOFs.

3.2.5. Adsorption isotherm. Two of the most often used isotherm models, the Langmuir and Freundlich isotherm models, were employed to characterize the equilibrium adsorptive desalination data.

A linear equation for the Langmuir isotherm model is as follows:

$$\frac{1}{q_e} = \frac{1}{q_m K_L C_e} + \frac{1}{q_m} \quad (3)$$

A linear equation for the Freundlich isotherm model is as follows

$$\ln q_e = \ln K_F + \frac{1}{n} \ln C_e \quad (4)$$

Where, q_e (mg g^{-1}) expressed the equilibrium adsorptive desalination capacity, q_m (mg g^{-1}) is defined as the maximum adsorptive desalination capability of the MIL88A(Fe) MOFs, α-cordierite porous, and nZnO@MIL88A(Fe)@α-cordierite composites, C_e (mg L^{-1}) is defined as the equilibrium concentration, K_L (mg L^{-1}) describes the Langmuir constant, n and K_F describes Freundlich constants.

Fig. 8(a and b) and Table 2 exhibited the Langmuir and Freundlich adsorption isotherm model for the MIL88A(Fe) MOFs, α-cordierite porous, and nZnO@MIL88A(Fe)@α-cordierite composites. Fig. 8(a and b) also exhibited a Langmuir isotherm plot having a correlation coefficient (R^2) of 1, which was greater than 0.9910 (R^2 value obtained from the Freundlich isotherm Model), hence, describing that the information derived for the adsorptive desalination phenomena fitted well into the Langmuir Model.

3.2.6. Kinetic study. Eqn (5) defines the pseudo-first-order kinetic model.

$$\ln K(q_e - q_t) = \ln q_e - K_1' \quad (5)$$

Eqn (6) defines the pseudo-second-order kinetic model.

$$\frac{t}{q} = \frac{1}{K_2 q_e^2} + \left(\frac{1}{q_e}\right) \times t \quad (6)$$

Where, q_t (mg g^{-1}) and q_e (mg g^{-1}) are adsorptive desalination capability at the time of interval t (min) and equilibrium. K_1 (min^{-1}) defines the kinetic rate constant describing the pseudo-first-order, and K_2 (g mg^{-1} min^{-1}) defines the kinetic rate constant describing the pseudo-second-order model.

Fig. 9 and Table 3 exhibited that adsorptive desalination of NaCl by prepared composites was fitted into a pseudo-second-order kinetic model.

3.2.7. Reusability or regeneration/adsorption–desorption study. The regeneration phenomena of porous α-Cordierite,

Table 2 Isothermal parameters for MIL88A(Fe) MOFs, α-cordierite porous ceramic, and nZnO@MIL88A(Fe)@α-cordierite composites

Isotherm models	Parameters	Values
MIL88A(Fe) MOF		
Langmuir isotherm model	q_e (mg g^{-1})	79
	K_L (mg L^{-1})	0.098
	R^2	0.9926
Freundlich isotherm model	K_F (mg g^{-1})	3.73
	n	1.03
	R^2	0.9829
α-Cordierite porous (ceramics)		
Langmuir isotherm model	q_e (mg g^{-1})	332
	K_L(mg L^{-1})	0.0245
	R^2	0.9983
Freundlich isotherm model	K_f (mg g^{-1})	16.92
	n	0.1729
	R^2	0.9877
nZnO@MIL88 (Fe)@α-cordierite composites		
Langmuir isotherm model	q_e (mg g^{-1})	473
	K_L(mg L^{-1})	3.25
	R^2	1
Langmuir isotherm model	K_f (mg g^{-1})	109.73
	n	3.65
	R^2	0.9910

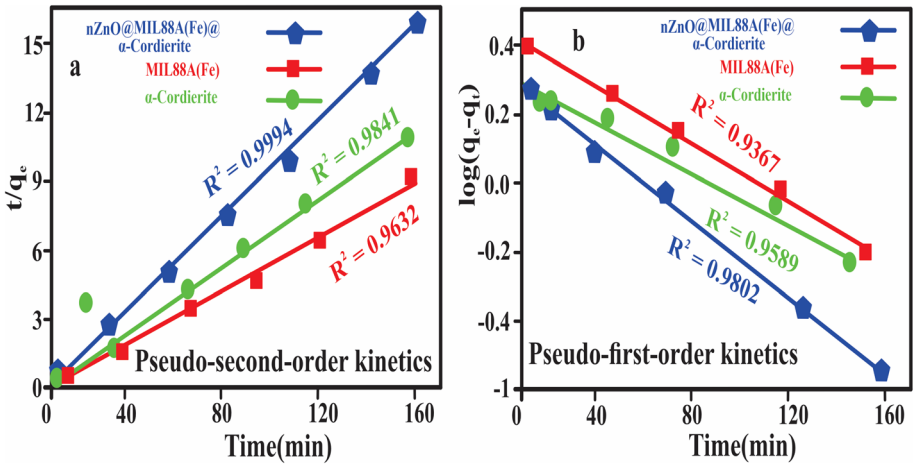

Fig. 9 Kinetic study, Pseudo-second-order (b) and pseudo-first-order (b).

Table 3 Kinetic parameters for MIL88A (Fe) MOFs, α-cordierite porous ceramic, and nZnO@MIL88A(Fe)@α-cordierite composites

Kinetic model	Parameters	Values
MIL88A(Fe)MOF		
Pseudo-first-order	q_e (mg g^{-1})	1.72
	K_1 (min^{-1})	0.0065
	R^2	0.9367
Pseudo-second-order	q_e (mg g^{-1})	0.85
	K_2 (g mg^{-1} min^{-1})	0.3
	R^2	0.9632
α-Cordierite porous (ceramics)		
Pseudo-first-order	q_e (mg g^{-1})	35.66
	K_1 (min^{-1})	7.36
	R^2	0.9589
Pseudo-second-order	q_e (mg g^{-1})	48.11
	K_2 (g mg^{-1} min^{-1})	3.40
	R^2	0.9841
nZnO@MIL88A(Fe)@α-cordierite composites		
Pseudo-first-order	q_e (mg g^{-1})	103.5
	K_1 (min^{-1})	0.006
	R^2	0.9802
Pseudo-second-order	q_e (mg g^{-1})	88.02
	K_2 (g mg^{-1} min^{-1})	7.3
	R^2	0.9994

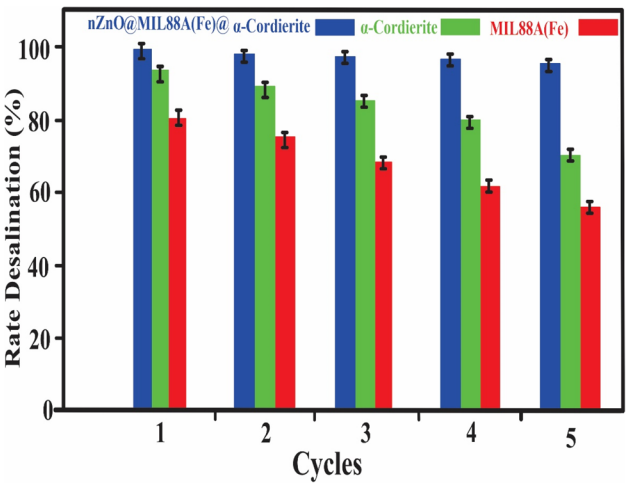

Fig. 10 Reusability or regeneration/Adsorption–desorption study of MIL88A(Fe) MOFs, α-cordierite porous ceramic, and nZnO@MIL88A(Fe)@α-cordierite composite.

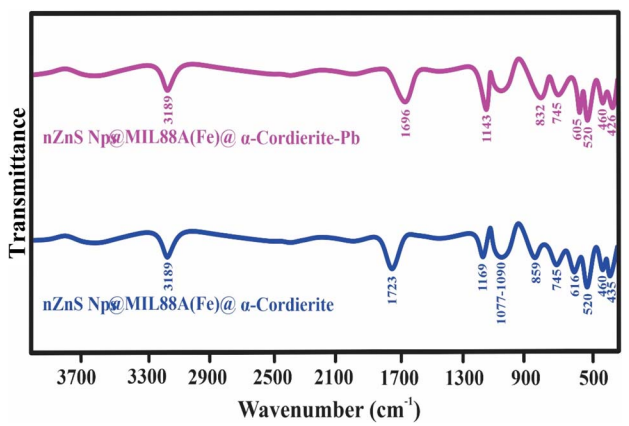

Fig. 11 FTIR spectra of nZnO@MIL88A(Fe)@α-cordierite composite before or after adsorptive desalination.

MIL88A(Fe), and nZnO@MIL88A(Fe)@α-cordierite composites are very significant from an economical perspective that is dependent on the desorption process of reagents. The composites that absorbed NaCl ions were bathed in DI water after the completion of each cycle to be reused. Fig. 9 showed that an adsorptive desalination rate of nZnO@MIL88A(Fe)@α-cordierite composite was only decreased by 4% as the maximum loss after 5 consecutive cycles. Fig. 10 also exhibited that the adsorptive desalination efficiency of nZnO@MIL88A(Fe)@α-cordierite composite was greater than porous α-cordierite and MIL88A(Fe).

3.2.8. Adsorption mechanism. Fig. 11 exhibited the FTIR pattern of nZnO@MIL88A(Fe)@α-cordierite composite before

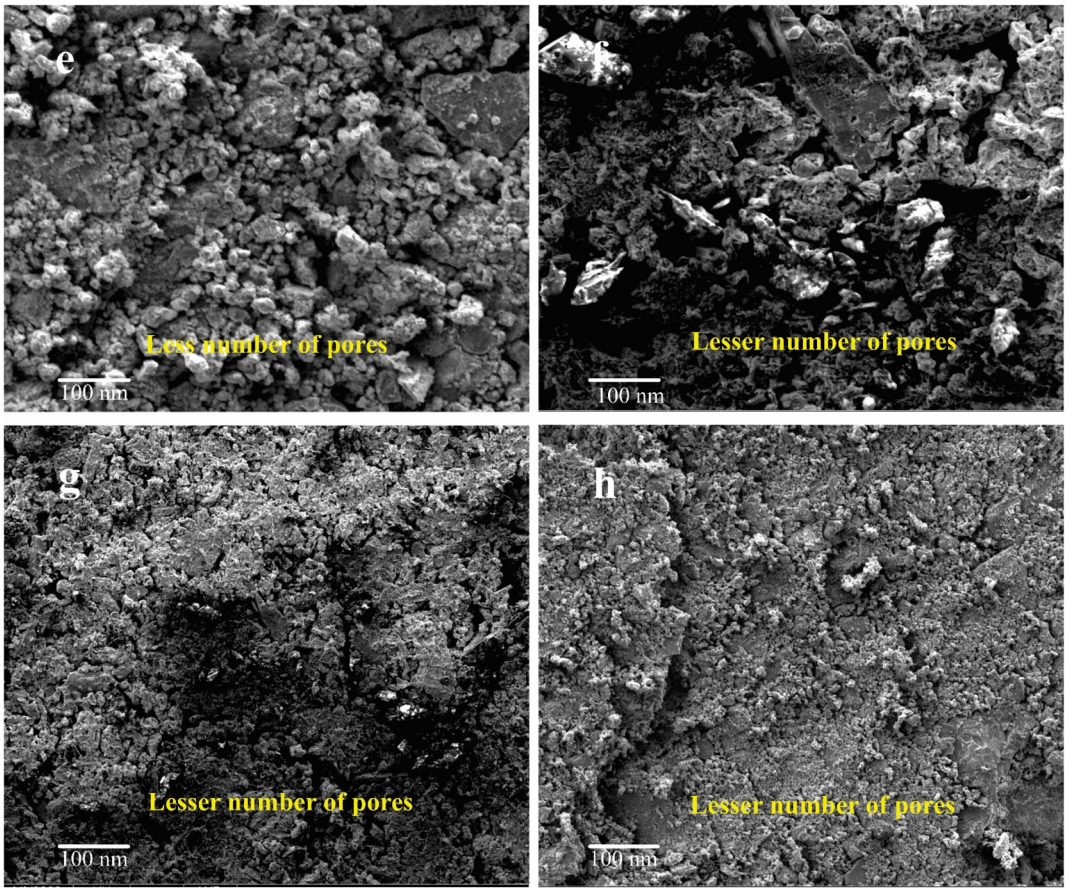

Fig. 12 SEM images of MIL88A(Fe) MOFs (e), ZnO NPs (f), α-cordierite porous ceramic (g), and nZnO@MIL88A(Fe)@α-cordierite composites (h) after adsorptive desalination.

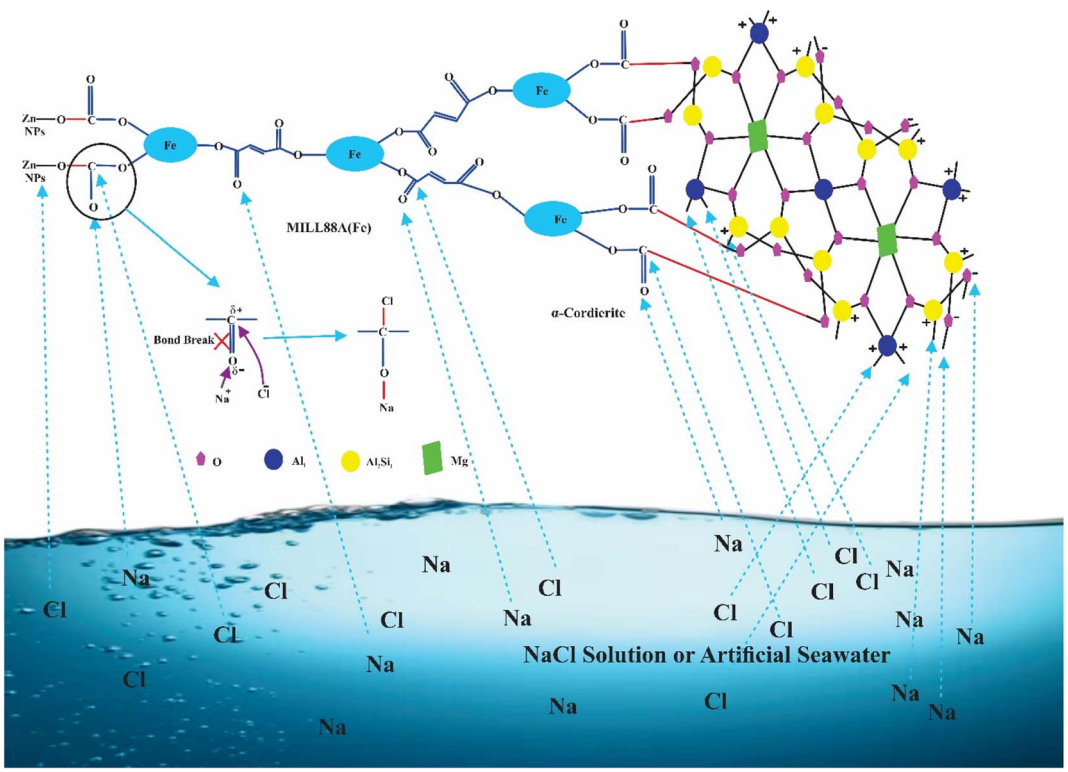

Fig. 13 The possible mechanism of adsorptive desalination.

Table 4 Comparison of rate of adsorptive desalination with previously reported materials

Material used	Desalination time	Removal rate (%)	Ref.
(MOF-Alg(Cu)) beads	30 min	85	15,16
MOF-808-EDTA	30 min	95	41
PDMVBA-MIL121	5 h	80	42
nZnO@MIL88A(Fe)@α-cordierite composite	13 min	99	This work

or after adsorptive desalination. In the FTIR spectra of nZnO@MIL88A(Fe)@α-cordierite composite after adsorptive desalination, two regions experienced clear changes. The first region is around 1000–2000 attributed to the carbonyl group (C═O), and AlO stretching in the nZnO@MIL88A(Fe)@α-cordierite composite shifted to the lower number and also confirms the interaction among C═O and AlO and Na and Cl as exhibited in Fig. 13. In the second region (400–900), the peak around 852 (SiO), 616 (ZnO), and 435 (ZnO) cm^{-1} also shifted to the lower wavenumbers 832, 605, and 426 cm^{-1}, suggesting the interaction of SiO and ZnO with Na and Cl.

MIL88A(Fe), ZnO NPS, α-cordierite ceramic, and nZnO@MIL88A(Fe)@α-cordierite composites were studied after adsorption of NaCl, and the outcomes exhibited in Fig. 12(e–h). By comparing SEM micrographs, we can conclude that the micro and mesoporous pores cavities of MIL88A(Fe) MOFs, ZnO nanoparticles, α-cordierite ceramic, and nZnO@MIL88A(Fe)@α-cordierite composites were filled after adsorptive desalination of NaCl and thus, decrease in the number of the pores. The rate of adsorption is primarily based on the number of pores.[39] The surface area of MIL88A(Fe), ZnO NPS, α-cordierite ceramic, and nZnO@MIL88A(Fe)@α-cordierite composites were also decreased due to the decrease in the number of micro and mesopores, and the rate of adsorptive desalination was decreased due to the decrease in the surface area. Physical and chemical adsorption is involved in the adsorption mechanism and similar result was reported by Zhang, Li, *et al.*[40]

3.2.9. Comparative analysis. A comparative study was performed to examine the potential use of nZnO@MIL88A(Fe)@α-cordierite composites in the efficient and rapid desalination of NaCl from seawater. A summary table was accomplished to describe the advantages of composite over other materials for the efficient and rapid removal of NaCl. Table 4 exhibited that nZnO@MIL88A(Fe)@α-cordierite composites exhibited higher or rapid desalination as compared to the previous literature.

4. Conclusion

In this research work, an excellent salt adsorbent, that is nZnO@MIL88A(Fe)@α-cordierite composite, was reported. Microporous nZnO@MIL88A(Fe)@α-cordierite composite was synthesized using a greener-microwave assisted approach. The synthesized composite exhibited high adsorptive desalination capacity for NaCl solution or artificial seawater. The obtained equilibrium data is well fitted in the Langmuir isotherm equation indicating monolayer desalination on the surface of nZnO@MIL88A(Fe)@α-cordierite composite. The kinetic study demonstrated that adsorptive desalination was well fitted to the Pseudo-second-order. According to the results of the present study, the nZnO@MIL88A(Fe)@α-cordierite composite is an excellent composite material for the removal of NaCl solution or artificial solution.

Conflicts of interest

The authors declare that they have no known competing financial interests or personal relationships that could have appeared to influence the work reported in this paper.

Acknowledgements

All authors acknowledge the School of Chemistry, Minhaj University Lahore for providing a platform for this work.

References

1 N. C. Darre and G. S. Toor, Desalination of water: a review, *Curr. Pollut. Rep.*, 2018, **4**, 104–111.
2 P. Goh, A. Ismail and B. Ng, Carbon nanotubes for desalination: Performance evaluation and current hurdles, *Desalination*, 2013, **308**, 2–14.
3 B. Arora and P. Attri, Carbon nanotubes (CNTs): a potential nanomaterial for water purification, *J. Compos. Sci.*, 2020, **4**, 135.
4 S. Kar, R. Bindal and P. Tewari, Carbon nanotube membranes for desalination and water purification: Challenges and opportunities, *Nano today*, 2012, **7**, 385–389.
5 M. O. Mavukkandy, C. M. Chabib, I. Mustafa, A. Al Ghaferi and F. AlMarzooqi, Brine management in desalination industry: From waste to resources generation, *Desalination*, 2019, **472**, 114187.
6 A. Panagopoulos, K.-J. Haralambous and M. Loizidou, Desalination brine disposal methods and treatment technologies-A review, *Sci. Total Environ.*, 2019, **693**, 133545.
7 A. Al-Karaghouli and L. L. Kazmerski, Energy consumption and water production cost of conventional and renewable-energy-powered desalination processes, *Renewable Sustainable Energy Rev.*, 2013, **24**, 343–356.
8 J. Zhao, L. Ren, Q.-b. Chen, P. Li and J. Wang, Fabrication of cation exchange membrane with excellent stabilities for electrodialysis: A study of effective sulfonation degree in ion transport mechanism, *J. Membr. Sci.*, 2020, **615**, 118539.
9 S. Lin, Energy efficiency of desalination: fundamental insights from intuitive interpretation, *Environ. Sci. Technol.*, 2019, **54**, 76–84.
10 S.-Y. Pan, A. Z. Haddad, A. Kumar and S.-W. Wang, Brackish water desalination using reverse osmosis and capacitive deionization at the water-energy nexus, *Water Res.*, 2020, **183**, 116064.
11 M. Al-Shammiri and M. Safar, Multi-effect distillation plants: state of the art, *Desalination*, 1999, **126**, 45–59.
12 D. L. Shaffer, L. H. Arias Chavez, M. Ben-Sasson, S. Romero-Vargas Castrillón, N. Y. Yip and M. Elimelech, Desalination

and reuse of high-salinity shale gas produced water: drivers, technologies, and future directions, *Environ. Sci. Technol.*, 2013, **47**, 9569–9583.

13 D. Brogioli, F. La Mantia and N. Y. Yip, Thermodynamic analysis and energy efficiency of thermal desalination processes, *Desalination*, 2018, **428**, 29–39.

14 S. Porada, R. Zhao, A. Van Der Wal, V. Presser and P. Biesheuvel, Review on the science and technology of water desalination by capacitive deionization, *Prog. Mater. Sci.*, 2013, **58**, 1388–1442.

15 E. Wibowo, M. Rokhmat and M. Abdullah, Reduction of seawater salinity by natural zeolite (Clinoptilolite): Adsorption isotherms, thermodynamics and kinetics, *Desalination*, 2017, **409**, 146–156.

16 S. J. Lee, T. Hann and S. H. Park, Seawater desalination using MOF-incorporated Cu-based alginate beads without energy consumption, *ACS Appl. Mater. Interfaces*, 2020, **12**, 16319–16326.

17 S. Dang, Q.-L. Zhu and Q. Xu, Nanomaterials derived from metal–organic frameworks, *Nat. Rev. Mater.*, 2017, **3**, 1–14.

18 S. Yuan, J.-S. Qin, J. Li, L. Huang, L. Feng, Y. Fang, C. Lollar, J. Pang, L. Zhang and D. Sun, Retrosynthesis of multi-component metal–organic frameworks, *Nat. Commun.*, 2018, **9**, 1–11.

19 W.-T. Koo, J.-S. Jang and I.-D. Kim, Metal–organic frameworks for chemiresistive sensors, *Chem*, 2019, **5**, 1938–1963.

20 Z. Gu, L. Chen, B. Duan, Q. Luo, J. Liu and C. Duan, Synthesis of Au@ UiO-66 (NH 2) structures by small molecule-assisted nucleation for plasmon-enhanced photocatalytic activity, *Chem. Commun.*, 2016, **52**, 116–119.

21 Q.-L. Zhu and Q. Xu, Metal–organic framework composites, *Chem. Soc. Rev.*, 2014, **43**, 5468–5512.

22 D. Pang, C.-C. Wang, P. Wang, W. Liu, H. Fu and C. Zhao, Superior removal of inorganic and organic arsenic pollutants from water with MIL-88A (Fe) decorated on cotton fibers, *Chemosphere*, 2020, **254**, 126829.

23 J. W. Jun, M. Tong, B. K. Jung, Z. Hasan, C. Zhong and S. H. Jhung, Effect of central metal ions of analogous metal–organic frameworks on adsorption of organoarsenic compounds from water: plausible mechanism of adsorption and water purification, *Chem.–Eur. J.*, 2015, **21**, 347–354.

24 Y. H. Teow and A. W. Mohammad, New generation nanomaterials for water desalination: A review, *Desalination*, 2019, **451**, 2–17.

25 R. Goren, H. Gocmez and C. Ozgur, Synthesis of cordierite powder from talc, diatomite and alumina, *Ceram. Int.*, 2006, **32**, 407–409.

26 M. Nadafan and R. Majidi, Study of optical constants and dielectric properties of nanocrystalline α-cordierite ceramic, *J. Asian Ceram. Soc.*, 2020, **8**, 502–509.

27 D. Feng, K. Wang, Z. Wei, Y.-P. Chen, C. M. Simon, R. K. Arvapally, R. L. Martin, M. Bosch, T.-F. Liu and S. Fordham, Kinetically tuned dimensional augmentation as a versatile synthetic route towards robust metal–organic frameworks, *Nat. Commun.*, 2014, **5**, 1–9.

28 G. Nagaraju, S. Prashanth, M. Shastri, K. Yathish, C. Anupama and D. Rangappa, Electrochemical heavy metal detection, photocatalytic, photoluminescence, biodiesel production and antibacterial activities of Ag–ZnO nanomaterial, *Mater. Res. Bull.*, 2017, **94**, 54–63.

29 V. S. Bhat, T. Tilakraj, M. K. Patil, V. Pujari and S. R. Inamdar, in *Tilte2022*, IOP Publishing, 2022.

30 M. E. Mahmoud, M. F. Amira, S. M. Seleim and A. K. Mohamed, Amino-decorated magnetic metal-organic framework as a potential novel platform for selective removal of chromium (Vl), cadmium (II) and lead (II), *J. Hazard. Mater.*, 2020, **381**, 120979.

31 R. Petrović, D. Janaćković, S. Zec, S. Drmanić and L. Kostić-Gvozdenović, Crystallization behavior of alkoxy-derived cordierite gels, *J. Sol-Gel Sci. Technol.*, 2003, **28**, 111–118.

32 M. K. Naskar and M. Chatterjee, A novel process for the synthesis of cordierite (Mg2Al4Si5O18) powders from rice husk ash and other sources of silica and their comparative study, *J. Eur. Ceram. Soc.*, 2004, **24**, 3499–3508.

33 A. S. Majumdar and G. Mathew, Raman-infrared (IR) spectroscopy study of natural cordierites from Kalahandi, Odisha, *J. Geol. Soc. India*, 2015, **86**, 80–92.

34 I. Janković-Častvan, S. Lazarević, D. Tanasković, A. Orlović, R. Petrović and D. Janaćković, Phase transformation in cordierite gel synthesized by non-hydrolytic sol–gel route, *Ceram. Int.*, 2007, **33**, 1263–1268.

35 C. Luan, D. Yuan, X. Duan, H. Sun, G. Zhang, S. Guo, Z. Sun, D. Pan, X. Shi and Z. Li, Synthesis and characterization of Co_{2+}: $MgAl_2O_4$ nanocrystal, *J. Sol-Gel Sci. Technol.*, 2006, **38**, 245–249.

36 P. Lee, H. Suematsu, T. Yano and K. Yatsui, Synthesis and characterization of nanocrystalline MgAl2O4 spinel by polymerized complex method, *J. Nanopart. Res.*, 2006, **8**, 911–917.

37 S. J. Lee and W. M. Kriven, Crystallization and densification of nano-size amorphous cordierite powder prepared by a PVA solution-polymerization route, *J. Am. Ceram. Soc.*, 1998, **81**, 2605–2612.

38 A. Husen, Gold nanoparticles from plant system: synthesis, characterization and their application, in *Nanoscience and plant–soil systems*, Springer, 2017, pp. 455–479.

39 A. Bukhari, I. Ijaz, H. Zain, E. Gilani, A. Nazir, A. Bukhari, S. Raza, S. Hussain, S. S. Alarfaji and Y. Naseer, Removal of Eosin dye from simulated media onto lemon peel-based low cost biosorbent, *Arabian J. Chem.*, 2022, **15**, 103873.

40 L. Zhang, P. Ma, L. Dai, S. Li, W. Yu and J. Guan, *In situ* crystallization and growth of TiO 2 nanospheres between MXene layers for improved adsorption and visible light photocatalysis, *Catal. Sci. Technol.*, 2021, **11**, 3834–3844.

41 C. Ji, H. Yu, J. Lu, Y. Ren, L. Lv and W. Zhang, High-efficiency and sustainable desalination using thermo-regenerable MOF-808-EDTA: temperature-regulated proton transfer, *ACS Appl. Mater. Interfaces*, 2021, **13**, 23833–23842.

42 R. Ou, H. Zhang, J. Wei, S. Kim, L. Wan, N. S. Nguyen, Y. Hu, X. Zhang, G. P. Simon and H. Wang, Thermoresponsive amphoteric metal–organic frameworks for efficient and reversible adsorption of multiple salts from water, *Adv. Mater.*, 2018, **30**, 1802767.